COMMUNICATION

Check for updates

A nanofibrous bacterial cellulose–carboxymethyl cellulose composite with high wet strength and active ester-mediated stable tissue adhesion in dynamic environments

Donghyun Hwang,[a] Donghyeok Kang, [iD]†[a] Kiho Sung [iD]†[a] and Sungchul Shin [iD]*[ab]

Tissue adhesives provide a minimally invasive alternative to sutures and staples, but achieving strong and durable adhesion on wet and dynamically deforming tissues remains a major challenge. Water disrupts interfacial bonding, and repeated deformation accelerates delamination, limiting the performance of existing synthetic and natural polymer systems. Here, we introduce a fully natural tissue adhesive based on a hybrid composite of bacterial cellulose (BC) and carboxymethyl cellulose (CMC) that integrates mechanical robustness with chemical reactivity. A three-dimensional BC nano-fiber network provides wet-resistant structural stability and pre-serves its layered architecture after chemical processing, while CMC chains functionalized with *N*-hydroxysuccinimide (NHS) ester and citric acid crosslinks enable rapid covalent bonding with tissue surfaces. This combination yields fast wet adhesion (∼10 s), high shear strength on skin and heart tissues (∼25 kPa), and exceptional fatigue resistance, maintaining interfacial integrity over more than 300 deformation cycles. The BC/CMC tissue adhesive also supports long-term cell viability, confirming its cytocompatibility. Further-more, kirigami-inspired laser-cut designs enable conformal, strain-accommodating adhesion on highly compliant tissues such as the lungs. Together, this natural polymer hybrid strategy provides a versatile and biocompatible platform for reliable sealing and repair on wet, dynamically moving biological surfaces.

New concepts

Achieving reliable wet adhesion is difficult because many polymer-based adhesives lose mechanical integrity when their networks swell in hydrated environments. To address this trade-off, we introduce a hybrid structural concept where carboxymethyl cellulose (CMC) is combined with a bacterial cellulose (BC) nanofibrous network that serves as a non-swelling backbone. This unique architecture allows the continuous BC scaffold to reach a wet strength near 500 kPa, about 450 times higher than crosslinked CMC aerogel adhesives, effectively preventing structural fail-ure during swelling and cyclic deformation. Beyond mechanical reinfor-cement, the nanofiber network of BC regulates CMC redistribution during freeze-drying to create a functional interface. By suppressing ice crystal growth, it forms a CMC-rich surface layer that increases the tissue contact area by about 50% and maximizes the density of *N*-hydroxy-succinimide (NHS) ester groups available for covalent bonding with tissue proteins. Demonstrating the efficacy of this dual-mechanism design, the resulting BC/CMC adhesive reaches wet shear strengths of about 25 kPa and maintains adhesion over more than 300 cycles of 20% strain. With kirigami patterning, our material accommodates the 40% strain of lung tissue. By combining BC-mediated mechanical stability with controlled interfacial chemistry, this novel approach supports wet-stable adhesion on dynamically moving tissues.

1. Introduction

A tissue adhesive is a biomaterial system that stably binds biological tissues through adhesion and sealing of wet inter-faces, unlike conventional sutures or staples.[1,2] It is widely used in hemostasis, wound closure, and organ reconstruction.[3–5] An ideal tissue adhesive should satisfy multiple criteria simultaneously: chemical bonding ability with tissue surfaces, mechanical compliance, wet adhesion stability, biodegrad-ability, and biocompatibility.[6–8] In particular, a tissue adhesive must retain its interfacial strength and long-term stability under hydrated physiological conditions and in dynamic envir-onments such as the continuously moving surfaces of the heart or lungs.[9,10] However, water molecules interfere with interfacial bonding, and external mechanical stress induces fatigue and delamination, making it challenging to achieve all these prop-erties in a single system.[11–13] To overcome these limitations, recent studies have pursued simultaneous enhancement of rapid wet adhesion and durability under cyclic deformation. Chemically, the introduction of catechol or L-3,4-dihydroxy-phenylalanine (DOPA) groups inspired by mussel adhesive proteins has enabled strong underwater adhesion.[14–16] Reactive functional groups such as aldehyde and *N*-hydroxysuccinimide

[a] *Department of Agriculture, Forestry, and Bioresources, Seoul National University, Seoul 08826, Republic of Korea. E-mail: hdh9766@snu.ac.kr, tinnnn_hyk11@snu.ac.kr, paswords@snu.ac.kr, sungssc@snu.ac.kr*

[b] *Research Institute of Agriculture and Life Sciences, Seoul National University, Seoul 08826, Republic of Korea*

† These authors contributed equally to this work.

(NHS) ester have also been employed to form amide or imine bonds with primary amines of tissue proteins, increasing the interfacial bond density.[11,17] Physically, rapid water absorption and capillary-driven contact provide efficient initial wet adhesion, while stress-distributing hierarchical porous networks are primarily responsible for enhancing fatigue resistant and conformal adhesion.[10,12] These chemical and physical strategies significantly enhance short-term wet adhesion and toughness, but most rely on synthetic polymers such as polyacrylamide, polyethylene glycol (PEG), and polyurethane. Although these materials offer high reactivity and structural tunability, they can undergo hydrolysis in physiological environments, generating low-molecular-weight byproducts such as acrylic acid or isocyanate, which may induce inflammatory responses or tissue irritation.[18–20] Moreover, incomplete biodegradability of some synthetic polymers poses a risk of long-term residue.[21] Therefore, next-generation tissue adhesives must transition from purely synthetic to natural polymer-based systems that ensure biological safety and structural robustness under wet conditions.

From this perspective, natural polymers have emerged as promising alternatives owing to their inherent biocompatibility and biological functionality. Fibrin, a protein-based adhesive derived from the blood coagulation process, forms a fibrous network through enzymatic reactions between thrombin and fibrinogen, enabling hemostasis and wound sealing.[22] Although fibrin gels exhibit excellent biocompatibility and support tissue regeneration, they suffer from low mechanical strength and poor wet stability, leading to detachment or rupture on highly deformable tissues such as the heart or lung.[2] To address these limitations, mussel-inspired adhesive systems were developed based on the underwater adhesion capability of marine mussel proteins.[23] The DOPA residue mediates hydrogen bonding, metal–ligand interactions, and oxidative covalent bonding, achieving strong wet adhesion.[24,25] Catechol-containing polymers mimicking this mechanism greatly increased the interfacial bond density compared with protein- or polysaccharide-based adhesives. However, DOPA-based systems still face challenges such as redox instability, pH-dependent performance, and high production costs.[14,24] As another natural polymer, carboxymethyl cellulose (CMC), a water-soluble cellulose derivative with carboxyl-functionalized hydroxyl groups, provides high biocompatibility, facile chemical modification, and cost-effective scalability.[26] The carboxyl groups of CMC can react with amine residues of tissue proteins through EDC/NHS-mediated coupling, and NHS-functionalized CMC adhesives have recently been explored as short-term wet adhesives.[27] Nevertheless, CMC-based adhesive layers rapidly lose mechanical integrity in wet environments due to swelling and disruption of the hydrogen-bonded network.

To address this issue, bacterial cellulose (BC) has gained increasing attention as a natural polymer exhibiting exceptional structural stability and biocompatibility. BC is a highly purified form of cellulose biosynthesized by microorganisms, consisting of an interconnected three-dimensional nanofibrous network with high porosity and water-holding capacity.[28] This continuous fibrous architecture maintains dimensional and mechanical stability even in hydrated states without structural collapse.[29] BC exhibits minimal cytotoxicity and excellent biocompatibility, and has been extensively studied for medical applications such as wound dressings, artificial skin, vascular grafts, and soft-tissue scaffolds.[30,31] These applications demonstrate that BC can remain stable in long-term physiological environments while promoting cell adhesion and tissue regeneration. Its porous nanofiber network facilitates cell attachment and proliferation, regulates moisture to prevent dehydration, and its abundant hydroxyl groups enable hydrogen bonding and protein adsorption without triggering inflammatory responses.[32,33] Together, these properties suggest that BC can serve not only as a protective dressing but also as a bioresponsive scaffold capable of dynamic interaction with living tissues.[34] However, the chemically inert nature of BC limits its ability to form covalent bonds with tissue proteins. Thus, a hybrid strategy is required to combine the structural stability and biocompatibility of BC with improved chemical reactivity for durable wet adhesion.

Here, we propose a natural polymer-based hybrid tissue adhesive that integrates the structural robustness of BC with the chemical reactivity of CMC. The chemically activated CMC rapidly forms covalent bonds with tissue proteins through NHS ester- and citric acid (CA)-mediated coupling, enabling fast and durable wet adhesion. Meanwhile, the densely entangled nanofiber network of BC not only provides mechanical stability and wet strength but also acts as a physical template that regulates CMC redistribution during freeze-drying, preserving a high density of CMC exposed at the adhesive surface. This surface enrichment increases the effective polymer–tissue contact area and directly enhances interfacial adhesion. As a result, the hybrid BC/CMC tissue adhesive demonstrates rapid, strong, and stable adhesion under wet conditions and maintains interfacial integrity even on dynamically deforming tissues such as the heart and lung. Moreover, the composite exhibits excellent cytocompatibility and long-term physiological stability without hindering cell attachment or proliferation. To address the large deformation and modulus mismatch characteristics of lung tissue, kirigami-inspired laser-cut patterns were introduced into the adhesive sheet, allowing the cuts to open and redistribute strain during stretching, thereby enabling deformation-compatible adhesion that prevents interfacial shear concentration and delamination even under ∼40% tensile strain. Accordingly, a hybrid approach that unites the structural stability of BC with the chemical reactivity of CMC offers a promising route to overcoming the long-standing limitations of wet adhesion on dynamically deforming tissues.

2. Results and discussion

2.1. Fabrication and characterization of the BC/CMC tissue adhesive sheet

To achieve stable adhesion under wet tissue environments, we designed a hybrid tissue adhesive sheet based on the porous

nanofibrous network structure of bacterial cellulose (BC). BC exhibits high mechanical strength and excellent biocompatibility, and its porous architecture acts as a physical template for hydrogel matrices. To complement this, we introduced carboxymethyl cellulose (CMC) to impart chemical functionality and enhanced interfacial stability through reactive bonding with *N*-hydroxysuccinimide (NHS) and citric acid (CA). We established a three-step fabrication process to integrate the structural stability of BC with the chemical reactivity of CMC (Fig. 1a). First, biosynthesized BC sheets were immersed in a 2 wt% aqueous CMC solution (average MW ≈ 90 kDa), allowing CMC chains to diffuse into the porous nanofibrous network structure of BC (Fig. 1a, panel i).[35] The quantitative analysis of the dry weight increase and the calculated CMC weight percentage revealed that CMC infiltration reached

saturation within 24 h, showing no significant difference compared to the 72 h condition. This confirms that a 24 h soaking period is sufficient to ensure stable infiltration into the BC network, which is critical for subsequent crosslinking (Fig. S1a and b, SI).[36] To further validate the spatial uniformity of infiltration, we analyzed the cross-sectional distribution of a fluorescent model molecule (FITC-dextran, average MW ≈ 150 kDa) using confocal laser scanning microscopy (CLSM). The resulting images and intensity profiles exhibited consistent fluorescence throughout the hydrogel depth, quantitatively verifying the spatial homogeneity of the infiltrated macromolecules (Fig. S1c and d, SI). Next, the carboxyl groups of the incorporated CMC were activated using 1-ethyl-3-(3-dimethylaminopropyl)carbodiimide (EDC) and reacted with NHS to form NHS ester groups (Fig. 1a, panel ii).[37] These activated
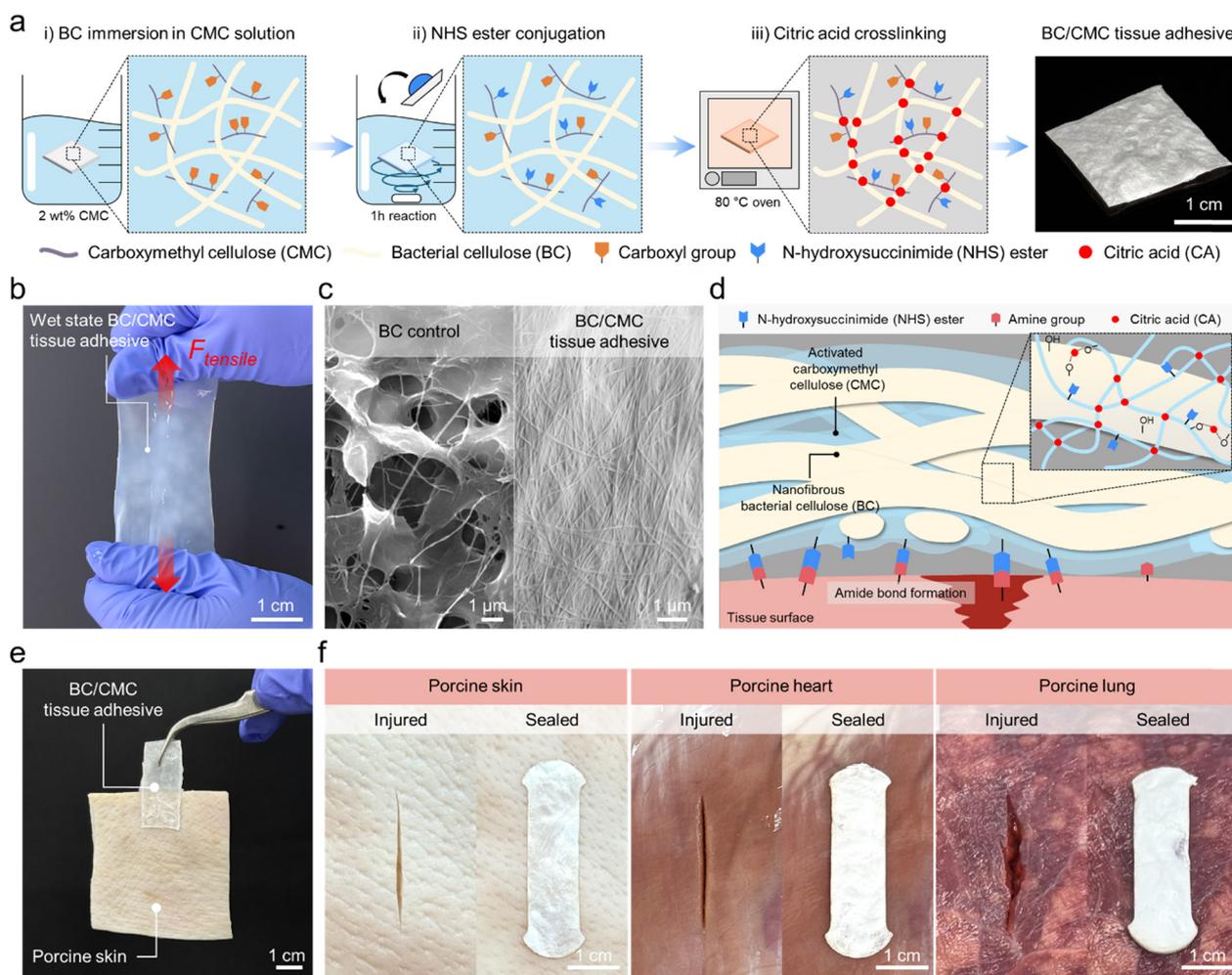

Fig. 1 Fabrication and characterization of the BC/CMC tissue adhesive sheet. (a) Schematic illustration of the three-step fabrication process: (i) incorporation of carboxymethyl cellulose (CMC) into the porous bacterial cellulose (BC) network, (ii) activation of carboxyl groups *via* *N*-hydroxysuccinimide (NHS) ester formation, and (iii) ester crosslinking with citric acid (CA) to yield the BC/CMC tissue adhesive sheet. (b) Photograph of the BC sheet demonstrating its mechanical integrity and flexibility under wet conditions. (c) SEM images comparing the BC control and the BC/CMC tissue adhesive sheet. (d) Schematic illustration of the adhesion mechanism, highlighting NHS-based covalent bonding and BC-supported CMC interface stabilization. (e) Photograph showing rapid and strong adhesion of the BC/CMC tissue adhesive sheet on porcine skin within 10 s under gentle pressure. (f) Photographs showing uniform and stable adhesion of the BC/CMC tissue adhesive sheet on various tissue surfaces, including porcine skin, heart, and lung.

sites serve as reactive functionalities that enable covalent bonding with primary amines of tissue proteins, thereby contributing to chemical adhesion. Finally, the BC/CMC-NHS composite containing CA was heated under high-humidity conditions to induce ester crosslinking between the carboxyl groups of CA and the hydroxyl groups of BC/CMC (Fig. 1a, panel iii).[38] This ester crosslinking prevents the loss of NHS activity during washing and suppresses excessive hydration under wet conditions, thereby improving structural stability.[39] Fourier-transform infrared (FTIR) spectroscopy confirmed both NHS activation and CA-based ester crosslinking. The CMC-NHS/CA tissue adhesive sheet exhibited a new peak near 1200 cm^{-1}, corresponding to the symmetric stretching of the C–N–C bond, indicating the formation of NHS esters (Fig. S2a, SI).[27] In addition, the BC/CMC-NHS/CA tissue adhesive sheet crosslinked with CA displayed a peak at 1713 cm^{-1}, attributed to the C=O stretching vibration of ester bonds (Fig. S2b, SI).[40] These spectral changes verify the formation of NHS-based activation and CA-mediated ester crosslinking within the composite network. Furthermore, a ferric ion-based colorimetric assay was employed to quantitatively evaluate the active NHS ester content. Following a well-established method,[41–43] the colorimetric response at 500 nm arises from the formation of ferric ion–NHS complexes following the hydrolysis of activated NHS ester groups. To provide a quantitative assessment, a calibration curve was first constructed using NHS standard solutions over a range of concentrations (Fig. S3a and b, SI). Using this assay, we quantified the active NHS ester content in the final BC/CMC adhesive sheet across various optimization conditions (Table S1 and Fig. S3c, SI). Notably, a significant amount of active NHS ester (0.014 mmol g^{-1}) was detected in the BC/CMC-NHS/CA sheet (sample 3), whereas negligible values were observed for the non-activated BC/CMC/CA control (samples 2 and 4). These quantitative results confirm the successful incorporation of NHS ester groups into the BC/CMC-based tissue adhesive system. Moreover, the detection of substantial active NHS groups in the washed BC/CMC-NHS/CA sheets (samples 3, 5, and 6) verifies that a significant fraction of esters preserved their reactivity, withstanding the humid conditions employed during thermal crosslinking.

Polymer-based tissue adhesives generally operate on wet tissue surfaces containing water and body fluids, where mechanical strength and interfacial stability decrease compared with dry conditions.[2] Due to this characteristic, adhesive layers on continuously deforming organs such as the heart and lung are prone to delamination or rupture.[44] To overcome this limitation, we introduced BC, which maintains high mechanical strength under hydrated conditions due to its entangled nanofibrous network structure. Consequently, BC is suitable for fabricating tissue adhesives that require strong mechanical reinforcement (Fig. 1b). Scanning electron microscopy (SEM) analysis was performed to examine the structural morphology of the tissue adhesives (Fig. 1c). First, the BC control prepared under identical conditions without CMC exhibited a highly porous network characterized by distinct open voids between the entangled nanofibers. In contrast, SEM images of the fabricated BC/CMC tissue adhesive sheet revealed that these micropores were partially filled with CMC, while the three-dimensional nanofibrous network of BC remained well preserved even after multiple processing steps such as immersion, drying, and heat treatment. This distinct morphological change indicates that CMC chains uniformly diffused into the BC network to form a fully integrated hybrid composite structure. The adhesion mechanism on tissue surfaces involves NHS esters on CMC reacting with primary amine groups of tissue proteins to form covalent amide bonds, while the BC nanofiber network serves as a structural template that organizes and supports the CMC coating layer at the interface, thereby enhancing the stability of wet adhesion (Fig. 1d). The fabricated BC/CMC tissue adhesive sheet rapidly adhered to tissue surfaces within approximately 10 s under gentle pressure, and the attached sheet remained firmly bonded even when lifted with forceps (Fig. 1e). This adhesion behavior results from the NHS esters reacting with the primary amine groups on wounded tissue surfaces to form stable amide bonds within minutes.[45] Uniform and stable adhesion was also observed on various tissue surfaces, including porcine skin, heart, and lung, indicating that the mechanical support of the BC nanofiber network structure and NHS-based covalent bonding collectively ensure robust interfacial stability (Fig. 1f).

2.2. Evaluation of mechanical properties and morphology of the BC/CMC tissue adhesive

Wound sites and organ surfaces are constantly exposed to wet environments containing blood, body fluids, and moisture, and tissue adhesives must maintain stable adhesion even on such hydrated surfaces.[46] However, under wet conditions, the mechanical strength and interfacial stability of adhesives are easily reduced, and on continuously deforming organs such as the heart or lung, the adhesive layer can fracture under tensile stress.[47] Therefore, the mechanical properties under wet conditions are key factors determining the durability and stability of adhesion in physiological environments.

BC maintains high wet strength due to its three-dimensional nanofibrous network structure, and this feature has led to its extensive use as a hydrogel scaffold for tissue regeneration.[48] To evaluate the tensile strength of the BC/CMC tissue adhesive under wet conditions, we prepared BC/CMC tissue adhesive, CMC tissue adhesive, and BC aerogel, and allowed them to fully swell in PBS solution (Fig. 2a). Even with citric acid-mediated thermal crosslinking, the CMC tissue adhesive reached an ultimate tensile strength of only ∼1.1 kPa in the wet state. This weak strength is attributed to the collapse of hydrogen-bonded networks during swelling and the lack of a mechanically entangled network capable of supporting external loads. In contrast, the BC aerogel maintained a high ultimate tensile strength of approximately 480–520 kPa, owing to the strong hydrogen bonding and mechanical entanglement between BC nanofibers that effectively support and distribute the applied stress. By comparison, the BC/CMC tissue adhesive showed a steeper initial slope compared with that of the BC aerogel, indicating reinforcement by the thermally crosslinked CMC chains within the BC nanofiber network (Fig. 2a). In contrast
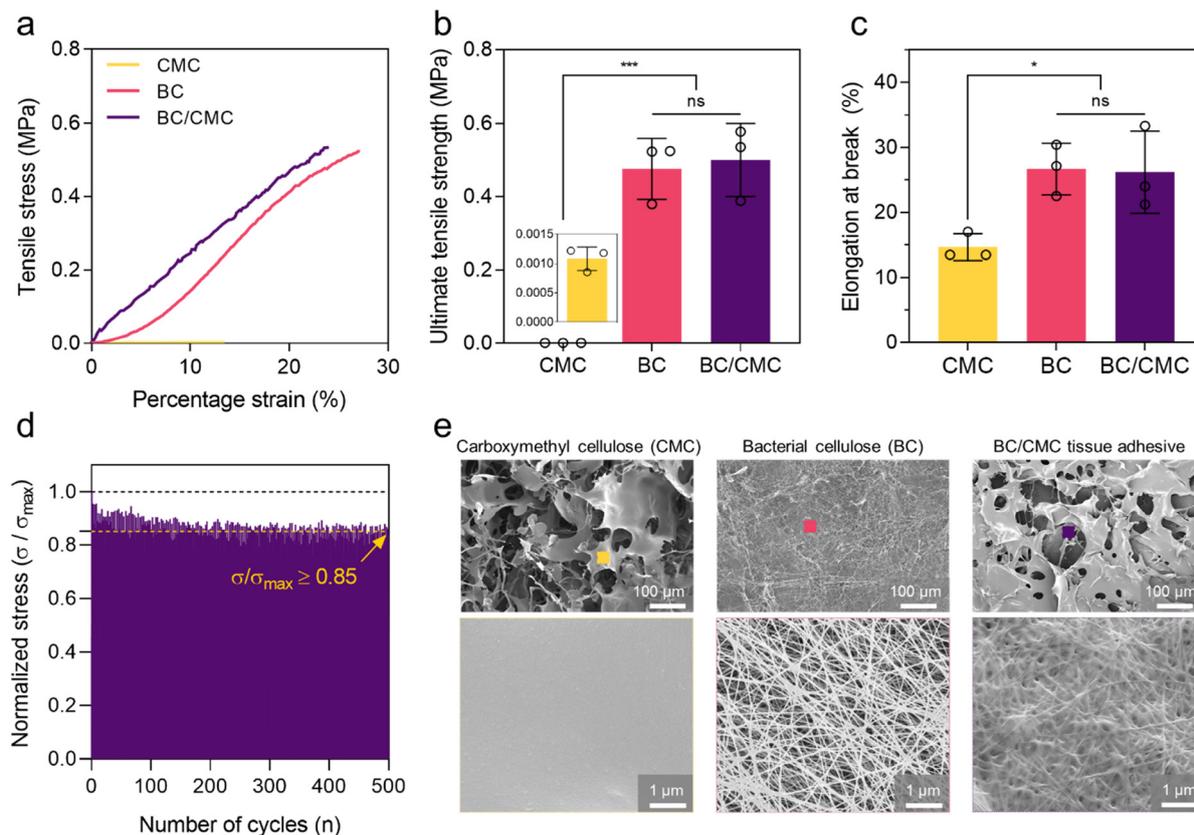
Fig. 2 Evaluation of mechanical properties and morphology of BC/CMC tissue adhesive. (a) Tensile stress–strain curves of CMC, BC, and BC/CMC tissue adhesive sheet measured under wet conditions. (b) Ultimate tensile strength and (c) elongation at break of each adhesive measured in the wet state. Data are presented as mean values ± SD (n = 3). (d) Cyclic tensile fatigue test results of the BC/CMC tissue adhesive performed at 10% strain for 500 cycles, demonstrating structural stability under repetitive loading. (e) SEM images of CMC, BC, and BC/CMC tissue adhesive at low and high magnifications. Low-magnification images (top) highlight overall surface morphology and pore structures, whereas high-magnification images (bottom) reveal smooth polymeric morphology in CMC and nanofibrous networks in BC-containing samples.

to the non-linear strain-hardening behavior of the BC aerogel, which reflects the progressive alignment of nanofibers, the BC/CMC tissue adhesive displayed a linear stress–strain relationship. This behavior is characteristic of a homogeneous elastic solid, indicating that the infiltrated CMC effectively fills the voids within the BC network to facilitate uniform stress transfer, preventing fiber reorientation. As a result, the ultimate tensile strength of the BC/CMC tissue adhesive increased approximately 450-fold and the elongation at break improved about 1.8-fold compared with the CMC tissue adhesive (Fig. 2b and c). This places our material as the strongest among natural polymer adhesives and demonstrates highly competitive mechanical performance even when compared to synthetic systems (Fig. S4 and Table S2, SI). For example, acrylic acid and catechol-functionalized chitosan hydrogels (PAA-NHS/ C-CS) with wet tensile strengths around 630 kPa have been reported.[49] Similarly, NHS-modified polyacrylic acid adhesive exhibits strengths above 120 kPa,[11] and graphene oxide-templated conductive hydrogels reach strengths of approximately 90 kPa.[50] In comparison, our BC/CMC tissue adhesive achieves a wet tensile strength of approximately 500 kPa, comparable to the highest-performing synthetic systems, while

relying exclusively on biocompatible and naturally derived polymers. Consequently, these results demonstrate that the BC/CMC tissue adhesive offers exceptional wet mechanical integrity and structural durability. In addition to tensile strength, we evaluated the elastic modulus to assess mechanical compatibility (Table S3, SI). The CMC tissue adhesive exhibited a significantly lower Young's modulus compared to the target tissues (skin, heart, and lung), indicating that CMC alone lacks the structural rigidity required for stable fixation. In contrast, the BC/CMC tissue adhesive demonstrated an enhanced modulus due to the reinforcement provided by the BC nanofibrous network, offering improved mechanical stability suitable for tissue application. Furthermore, to assess the structural stability of the adhesive under repetitive mechanical loading, we performed cyclic tensile fatigue tests at 10% strain. The BC/CMC tissue adhesive exhibited negligible hysteresis and a stress decay of only 15% after 500 cycles (Fig. 2d). This exceptional fatigue resistance confirms that the bulk network preserves its mechanical integrity for long-term applications in dynamic physiological environments.

To investigate the structural features responsible for the mechanical performance of each adhesive, we examined their surface microstructures using SEM (Fig. 2e). The CMC tissue

adhesive exhibited a rough surface with irregular macropores approximately 10–100 μm in size, formed by ice crystal growth and solvent removal during freeze-drying. In contrast, the BC aerogel maintained a highly dense surface structure. This result is attributed to the long aspect ratio of BC nanofibers, which entangle to form a robust three-dimensional network that resists displacement by growing ice crystals during freezing.[51] The BC/CMC tissue adhesive exhibited an intermediate morphology between the two materials, showing macropores partially filled with denser CMC-rich regions. This indicates the coexistence of CMC-induced porosity and BC-derived dense structures. At higher magnification, the CMC tissue adhesive showed smooth pore walls that freeze-dried water-soluble polymers typically show, whereas the BC aerogel clearly displayed a nanofibrous network composed of entangled nanofibers with diameters of 30–50 nm. This continuous nanofibrous architecture is a key factor responsible for maintaining high tensile strength in the wet state. Similar nanofibrous network structures were observed in the BC/CMC tissue adhesive, indicating that the BC nanofiber network remained structurally intact after the combined processes of CMC immersion, NHS/EDC reaction, and thermal crosslinking. This structural preservation demonstrates that the inherent stiffness of BC fibers is retained within the composite, ensuring mechanical reinforcement and effectively supporting and distributing the applied stress across the adhesive layer.

2.3. Interfacial adhesion performance and structural characterization of the BC/CMC tissue adhesive

Tissue adhesives must maintain stable adhesion even on tissue surfaces covered with water and body fluids, and they should be rapidly and easily applicable in actual surgical environments.[9] Our BC/CMC tissue adhesive formed rapid and stable adhesion on wet tissue surfaces within only 10 s of gentle pressure, demonstrating its potential for practical clinical use. Notably, a 1 cm^2 adhesive sheet was able to lift a 20 g piece of porcine skin, visually confirming its strong interfacial adhesion (Fig. 1e). This fast adhesion arises from the reaction between the NHS ester groups of CMC and the primary amine groups of tissue proteins, forming covalent amide bonds within minutes.[11,27] To quantitatively evaluate the interfacial adhesion, we performed lap-shear tests using porcine skin as a model tissue, which closely mimics the mechanical properties of human skin (Fig. 3a). The adhesives were applied to wet tissue surfaces, pressed for 10 s, and then subjected to shear loading. The CMC tissue adhesive exhibited a shear strength of approximately 13 kPa, comparable to previously reported CMC-NHS-based tissue adhesives (Fig. 3b).[27] Interestingly, the unmodified BC aerogel also exhibited a similar shear strength, which can be attributed to the rapid absorption of interfacial moisture by its porous structure and the physical interlocking provided by the nanofibrous network with its rough, high-surface-area fiber morphology. Notably, the non-activated BC/CMC aerogel (without NHS) also displayed a low shear strength comparable to that of the BC aerogel. This observation confirms that the simple physical combination of BC and CMC does not significantly enhance tissue adhesion, thereby isolating NHS-mediated

chemical bonding as the primary driver for high interfacial strength. In the hybrid BC/CMC tissue adhesive sheet, we optimized the NHS-EDC activation conditions and the CA-mediated thermal crosslinking parameters to enhance adhesion to skin tissue (Table S1 and Fig. S5, SI). We found that the formulation containing BC, 2% CMC, 0.2 M EDC, 0.2 M NHS, and 0.16% citric acid exhibited the highest shear strength, indicating that this combination provided the most effective balance between reactive NHS ester formation and sufficient crosslinking density. This critical role of active NHS esters is further substantiated by the quantitative analysis, which revealed that the superior lap-shear strength of the NHS-treated adhesive corresponds directly to its high content of active ester groups (Fig. S3c, SI). Under this optimized formulation, the hybrid BC/CMC tissue adhesive demonstrated a significantly higher shear strength of approximately 25 kPa, more than twice that of the BC aerogel, the BC/CMC aerogel, and the CMC tissue adhesive (Fig. 3b). This enhancement results from the synergistic combination of the mechanically supportive BC network and the covalent amide bonding induced by the NHS esters, which together increase the interfacial bond density.

Since the adhesion strength of tissue adhesives largely depends on the effective contact area with tissue, we compared the polymer surface area fraction of each adhesive sheet. SEM images were binarized to distinguish polymer regions (white) from pores (black), and the fraction of polymer area relative to the total surface was quantified (Fig. 3c and Fig. S6, SI). The BC and BC/CMC (without NHS) aerogels exhibited similar polymer area fractions. This suggests that, in the absence of NHS, effective crosslinking between BC and CMC was not achieved, as NHS activation is crucial for promoting the formation of ester crosslinks by citric acid.[27] In addition, the CMC tissue adhesive showed large macropores on the order of ∼10–50 μm formed by ice-crystal growth during freezing, resulting in a relatively low polymer surface area fraction of approximately 50%. In contrast, the BC/CMC tissue adhesive showed a markedly higher polymer surface area fraction of about 76%. This increase is attributed to the retention of CMC within the BC nanofiber network, leading to a greater amount of CMC exposed to the surface. We further analyzed cross-sectional SEM images to observe how polymer distribution varied with BC incorporation (Fig. 3d). The CMC tissue adhesive exhibited a continuous open-pore structure from the surface to the interior, whereas BC aerogel displayed an entangled nanofiber network arranged in a layer-by-layer architecture. We propose that this dense nanofibrous network acts as a physical mesh that restricts the movement of ice crystals during freezing, thereby preventing CMC from being displaced inward and maintaining a compact, homogeneous surface (Fig. 3e). In the BC/CMC tissue adhesive, CMC was partially distributed among the BC nanofibers, filling the pores and increasing the overall polymer density at the surface (Fig. 1c). This hybrid microstructure effectively enlarged the actual contact area with tissue surface and suggests that the BC nanofiber network remains structurally preserved after composite processing,
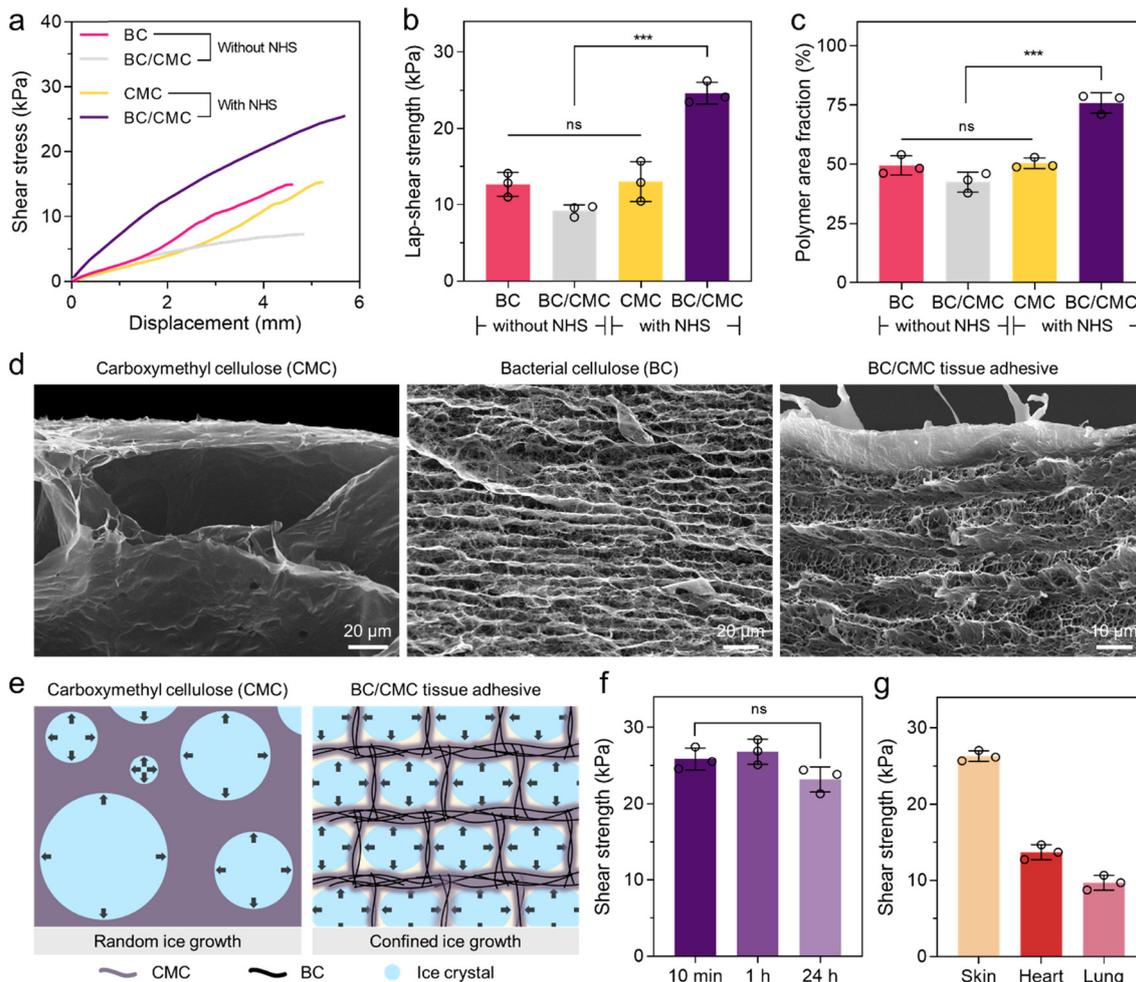
Fig. 3 Interfacial adhesion performance and structural characterization of BC/CMC tissue adhesive. (a) Representative shear stress–displacement curves obtained from lap-shear tests comparing the shear adhesion performance of BC and BC/CMC (without NHS) aerogels *versus* CMC and BC/CMC (with NHS) tissue adhesives on wet porcine skin. (b) Comparison of lap-shear strength among BC, BC/CMC (without NHS), CMC, and BC/CMC (with NHS) tissue adhesives under wet conditions. (c) Quantitative analysis of polymer surface area fraction calculated from binarized SEM surface images. (d) Cross-sectional SEM images of CMC, BC, and BC/CMC tissue adhesives showing differences in internal morphology and the layered nanofiber architecture. (e) Schematic illustration of the proposed microstructural mechanism by which the BC nanofiber network restricts ice-crystal growth during freezing, preserving a dense surface layer and enhancing polymer exposure for interfacial contact. (f) Shear strength of the BC/CMC tissue adhesive measured after 10 min, 1 h, and 24 h of adhesion on wet porcine skin. (g) Shear strength of the BC/CMC tissue adhesive across porcine skin, heart, and lung tissues under wet conditions. Data are presented as mean values $\pm$ SD (n = 3).

contributing to both mechanical support and enhanced adhesion efficiency.

To evaluate the long-term adhesion stability, we measured the shear strength of the BC/CMC tissue adhesive over different time points after adhesion (Fig. 3f and Fig. S7, SI). The shear strength values at 10 min, 1 h, and 24 h after application showed no significant differences, indicating that the amide bonds formed at the interface remained stable over time. These results suggest minimal reduction of adhesion due to NHS ester hydrolysis and confirm that the BC/CMC tissue adhesive maintains reliable adhesion stability even in prolonged wet environments. Next, we tested adhesion performance on different porcine tissues, including skin, heart, and lung (Fig. 3g and Fig. S8, SI). The BC/CMC tissue adhesive exhibited stable attachment across all tissues, with higher shear strength

observed on relatively firm tissues such as skin and heart. On the softer and more deformable lung tissue, a larger displacement was recorded during testing, reflecting the deformation of the tissue itself rather than detachment of the adhesive layer. To further elucidate the failure mechanism and mechanical integrity of the composite, we first examined the macroscopic failure behavior during lap-shear testing of various tissues (skin, heart, and lung). For all tissue types, interfacial failure was observed, in which the adhesive remained on one tissue substrate, while the opposing substrate exhibited a clean surface without residual adhesive (Fig. S9, SI). In addition, the fracture surfaces of the tissues after detachment were analyzed by SEM. The SEM images revealed clean tissue surfaces with no observable adhesive residue, confirming that the failure occurred primarily at the adhesive-tissue

interface (adhesive failure) rather than within the bulk adhesive (cohesive failure) (Fig. S10, SI). This behavior is attributed to the robust reinforcement provided by the BC nanofibrous network, which imparts high cohesive strength to the composite, preventing internal fracture even under high shear stress. Consequently, the BC/CMC tissue adhesive enables strong fixation and clean removal without leaving polymer debris that could potentially impede wound healing. Importantly, these post-detachment surfaces exhibited negligible morphological changes compared to the pristine state, confirming tissue safety without causing surface damage. These findings demonstrate that the BC/CMC tissue adhesive maintains stable adhesion under diverse tissue environments and can adapt to tissue deformation while preserving interfacial integrity. Collectively, this confirms its potential as a versatile and robust tissue adhesive applicable to skin, heart, and lung surfaces.

2.4. *In vitro* cytocompatibility evaluation of the BC/CMC tissue adhesive

Because tissue adhesives are in direct contact with living tissues, verifying their biocompatibility through cytotoxicity evaluation is essential.[52] To assess the cell viability and proliferation of the fabricated BC/CMC tissue adhesive, we performed Live/Dead and Alamar Blue assays using NIH-3T3 fibroblasts. We first examined the initial cell attachment and long-term survival using Live/Dead fluorescence imaging (Fig. 4a). On Day 1, cells were uniformly attached to both BC and BC/CMC samples, and almost no dead cells (red fluorescence) were observed. On the BC surface, cells were sparsely distributed at first but gradually proliferated and formed clusters over time. On the BC/CMC surface, cell density also increased progressively, although cell-to-cell connectivity and cell spreading appeared slightly more restricted than on BC. After seven days of culture, both samples exhibited abundant viable cells with minimal red fluorescence, confirming high cell viability and the absence of cytotoxic effects. These results demonstrate that both BC aerogel and BC/CMC tissue adhesive provide a stable surface microenvironment for long-term cell growth without inducing cytotoxicity. Quantitative analysis of the stained images further substantiated these findings (Fig. 4b). The calculated cell viability remained consistently high (exceeding 90%) across all groups throughout the 7-day culture period, with no significant statistical difference observed between the BC and BC/CMC samples. These results objectively confirm that the incorporation of CMC and the associated chemical modifications do not compromise the intrinsic biocompatibility of the BC nanofibrous network.

To quantitatively analyze cell metabolic activity, we performed an Alamar Blue assay (Fig. 4c). For all samples, fluorescence intensity gradually increased with culture time, reflecting enhanced cell proliferation and metabolism. On Day 1, no significant difference was observed between the BC and BC/CMC samples. By Day 4, both samples exhibited slightly higher fluorescence intensity compared to the tissue culture plate (TCP) control, confirming that the materials provide a cytocompatible environment that does not hinder cell proliferation. On Day 7, all samples exhibited comparable fluorescence intensity, indicating sustained cell viability and the absence of toxicity during long-term culture. Therefore, the BC/CMC tissue adhesive does not induce cytotoxic effects and stably
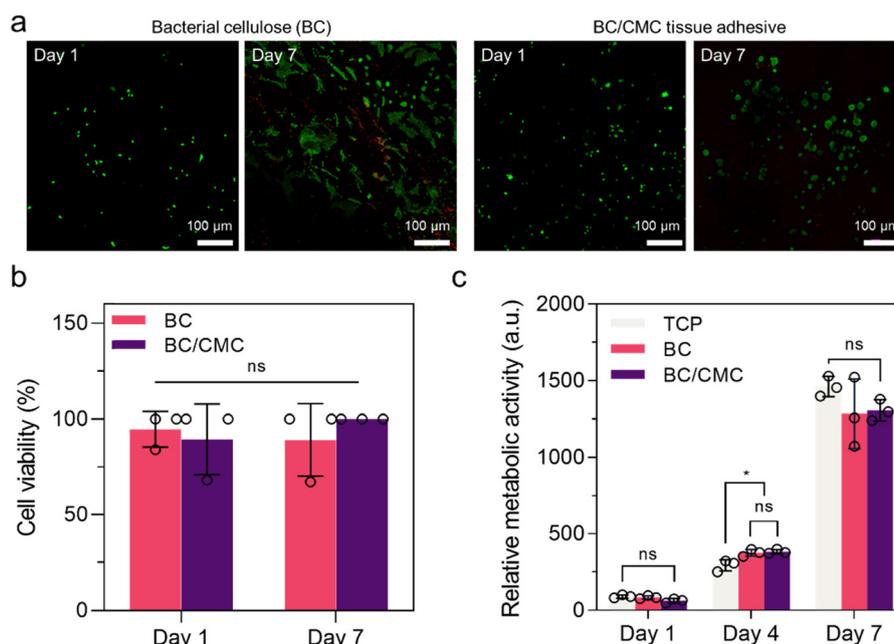

Fig. 4 *In vitro* cytocompatibility evaluation of the BC aerogel and BC/CMC tissue adhesive. (a) Live/Dead fluorescence images of NIH-3T3 fibroblasts cultured on the BC aerogel and BC/CMC tissue adhesive for 1 and 7 days. Green and red signals represent live and dead cells, respectively. (b) Quantitative analysis of cell viability calculated from the Live/Dead staining images of the BC aerogel and BC/CMC tissue adhesive. (c) Alamar Blue assay–based quantification of cell metabolic activity on the tissue culture plate (TCP), BC aerogel, and BC/CMC tissue adhesive at different culture times (Days 1, 4, and 7). Data are presented as mean values ± SD ($n = 3$).

supports NIH-3T3 fibroblast adhesion and proliferation. These findings confirm that the BC/CMC tissue adhesive is a cytocompatible material capable of maintaining a stable adhesive layer without interfering with cell growth or tissue regeneration *in vivo*-like conditions.

2.5. Cyclic-loading durability and kirigami-inspired structural customization of the BC/CMC tissue adhesive

To ensure stable application of tissue adhesives on dynamic organ surfaces such as the heart and lung, it is crucial to maintain structural integrity and adhesion strength under repeated mechanical deformation. To verify this, cyclic loading tests were performed using porcine heart tissue (Fig. 5a). Two pieces of heart tissue were bonded with each adhesive (CMC tissue adhesive, BC aerogel, and BC/CMC tissue adhesive) and subjected to 20% tensile strain under cyclic conditions to compare adhesion stability in dynamic tissue environments.

The CMC tissue adhesive exhibited a rapid load drop during the first loading cycle under wet conditions, and the adhesive layer fractured immediately (Fig. 5b). This failure resulted from water-induced swelling of CMC, which significantly reduced its mechanical strength, consistent with the previously observed low ultimate tensile strength of 1.1 kPa under wet conditions (Fig. 2b). In contrast, the BC aerogel sustained partial loads during the initial cycles but delaminated within the first cycle, leading to loss of adhesion (Fig. 5c). The measured maximum load was approximately 0.70 N, comparable to the lap-shear test result of 0.78 N under identical conditions, indicating that the tissue detachment originated from interfacial failure (Fig. S11, SI). Although the adhesive interface fractured, the intrinsic mechanical integrity of BC was maintained, confirming that interfacial bonding strength was the primary limiting factor. On the other hand, the BC/CMC tissue adhesive reached a steady-state load and maintained
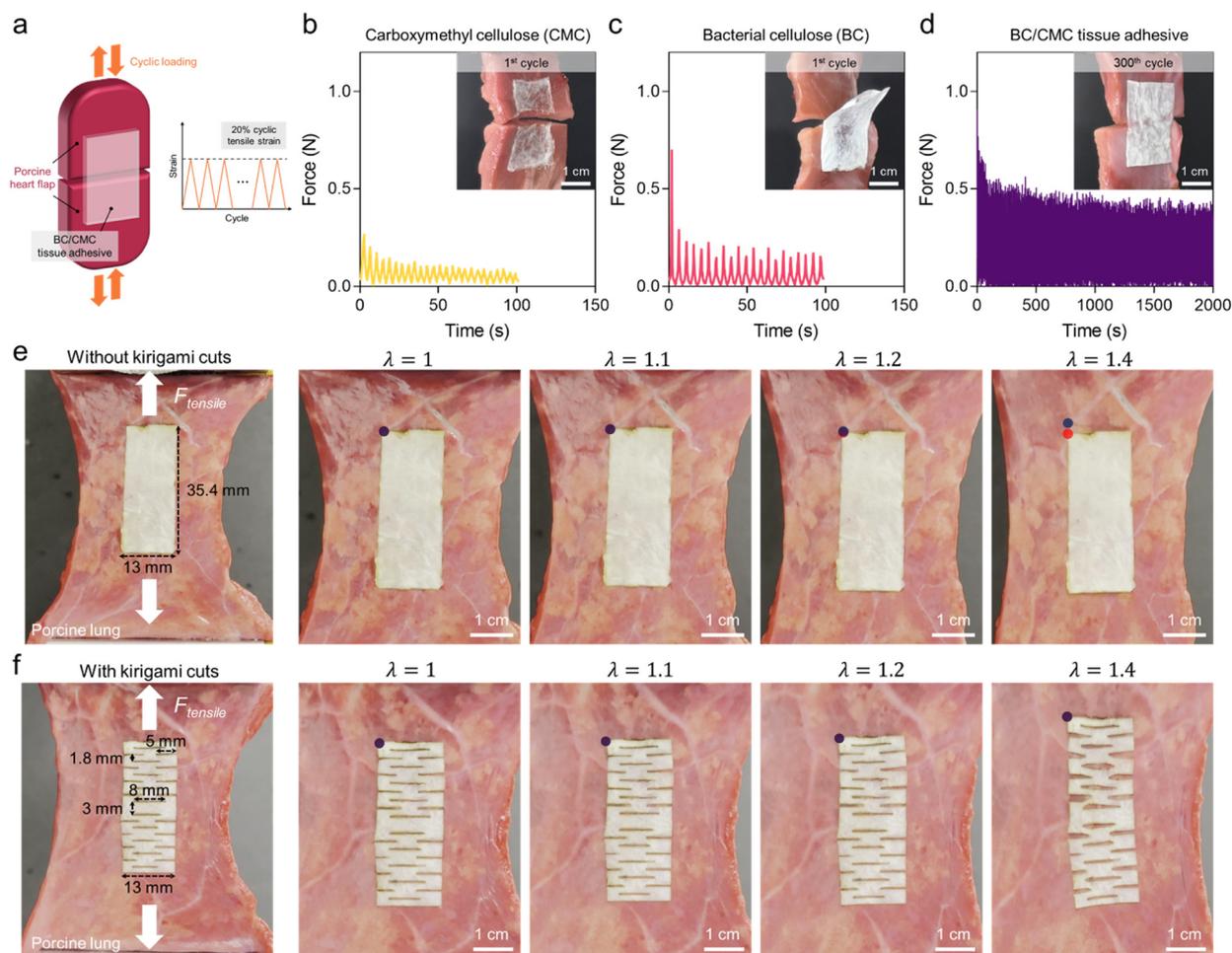

Fig. 5 Cyclic-loading durability and kirigami-inspired structural customization of the BC/CMC tissue adhesive. (a) Schematic illustration of the cyclic-loading test on porcine heart tissue, where two tissue flaps were bonded with CMC tissue adhesive, BC aerogel, or BC/CMC tissue adhesive and subjected to 20% cyclic tensile strain. (b) Load-time curve and photograph of the CMC tissue adhesive after cyclic loading. (c) Load-time curve and photograph of the BC aerogel after cyclic loading. (d) Load-time curve and photograph of the BC/CMC tissue adhesive after cyclic loading. (e) Photograph of the tensile test showing the relative displacement between the upper-left corner of the adhesive sheet (red marker) and a fixed point on the lung surface (blue marker) during applied deformation. (f) Photograph of the BC/CMC adhesive sheet featuring laser-cut kirigami patterns fabricated for deformation-accommodating structural design.

nearly constant stress over more than 300 cycles without load drop, delamination, or cracking (Fig. 5d). This remarkable fatigue durability is attributed to the synergistic effect between the mechanical reinforcement provided by the BC nanofiber network and the chemical bonding by CMC, which together relieve stress concentration and suppress interfacial failure under cyclic deformation. These results demonstrate that the BC/CMC tissue adhesive stably maintains both structure and adhesion under the cyclic deformation of heart tissue.

Meanwhile, lung tissue undergoes substantially larger cyclic volumetric deformations (approximately 20–50%) compared with the 15–25% strain typically observed in cardiac tissue, and its elastic modulus is also much lower, around 2 kPa compared with ~ 50 kPa for the heart (Table S3).[53] A large modulus contrast between a soft tissue and an adhesive sheet limits the ability of the sheet to deform synchronously with the tissue, leading to interfacial shear concentration and promoting delamination during extension.[54] Consequently, applying a simple rectangular-shaped adhesive sheet with an elastic modulus of approximately 4 MPa to the lung places the interface under mechanically unfavorable conditions due to pronounced mechanical discrepancy between the two materials. In deformation tests, the BC/CMC tissue adhesive sheet began to detach from the upper edge once the tensile strain exceeded approximately 20%. During stretching, the vertical dimension of the film changed minimally, whereas the distance between the upper-left corner of the sheet and a fixed point on the lung surface increased, confirming the onset of interfacial sliding and debonding (Fig. 5e). To enable stable adhesion under the large deformation characteristic of lung tissue, we introduced a kirigami-inspired structural design.[55] Kirigami patterns were precisely implemented into the adhesive sheet using a laser-cutting process (Fig. 5f), and interfacial behavior was evaluated under 40% tensile strain. In the kirigami-patterned sheet, the cut motifs progressively opened during stretching, allowing the sheet to extend in concert with the tissue. This deformation compatibility preserved interfacial integrity without noticeable delamination. Thus, the kirigami architecture provided an effective strategy for maintaining adhesion in tissue environments where modulus disparity and large deformation strongly promote interfacial failure. Furthermore, because clinical wounds vary widely in shape, size, and anatomical location, geometrical customizability is essential. Using the same laser cutting process, we fabricated adhesive sheets in diverse customized geometries, demonstrating the potential of this approach for patient-specific adhesive patches that conform to complex wound morphologies (Fig. S12, SI).

3. Conclusions

In this study, we developed a natural polymer-based tissue adhesive that maintains stable performance under wet and dynamically deforming physiological conditions. By integrating the mechanically robust nanofibrous network of bacterial cellulose (BC) with the chemically reactive carboxymethyl cellulose (CMC), the composite forms a structurally reinforced and chemically functional adhesive layer capable of enduring hydration, deformation, and interfacial stress. This hybrid structure achieved high tensile and shear strength in wet environments and preserved adhesion through more than 300 cycles of cyclic loading, demonstrating outstanding fatigue durability. The composite also retained its nanofibrous architecture throughout chemical processing and supported long-term cell attachment and proliferation, confirming excellent cytocompatibility. In addition, kirigami-inspired patterning enabled deformation-accommodating geometries suitable for soft organs such as the lung. Together, these findings establish a natural polymer strategy that unites structural stability, chemical reactivity, and biocompatibility within a single material platform. The BC/CMC system provides a practical design framework for bioadhesives capable of reliable sealing and repair on wet, dynamically moving tissues and offers a broadly applicable approach for engineering mechanically compliant and chemically functional biointerfaces.

4. Experimental

4.1. Materials

Komagataeibacter xylinus (*K. xylinus*, KACC 17012) was obtained from Korean Agricultural Culture Collection for bacterial cellulose (BC) biosynthesis. Sodium hydroxide (NaOH, ≥93%, Duksan, Korea) was used for the purification of BC. For the preparation of BC/CMC-NHS/CA tissue adhesive, sodium carboxymethylcellulose (CMC, MW ≈ 90 000, DS = 0.7, Sigma-Aldrich, USA), 2-morpholinoethanesulfonic acid hydrate (MES, ≥99%, Alfa Aesar, USA), 1-ethyl-3-(3-dimethylaminopropyl)carbodiimide hydrochloride (EDC, ≥98%, Acros Organics, USA), *N*-hydroxysuccinimide (NHS, ≥98%, Alfa Aesar, USA), and citric acid monohydrate (CA, ≥99.5%, Duksan, Korea) were used. All porcine tissue samples used for adhesion tests were purchased from a local supermarket.

4.2. Biosynthesis and purification of bacterial cellulose (BC)

K. xylinus was cultured in a mannitol-based medium composed of 2.5 wt% mannitol (≥99%, Samchun, Korea), 0.3 wt% bacto-peptone (Gibco, USA), and 0.5 wt% yeast extract (Gibco, USA). Cultivation was carried out in square Petri dishes at 28 °C for 4 days. After cultivation, BC pellicles (~ 3 mm thick) were purified by immersion in 1 wt% NaOH solution at room temperature for 24 h and subsequently rinsed with distilled water for 2 days to remove residual impurities. The cellulose fiber content in the purified BC was 0.7 wt%.

4.3. Preparation of the BC/CMC-NHS/CA tissue adhesive

CMC (2 wt%) was dissolved in 1 M MES buffer (pH 6), and BC pellicles (20 mm × 20 mm) were immersed in the solution at room temperature under gentle shaking (100 rpm) for 24 h to allow sufficient incorporation of CMC into the BC network. EDC and NHS were then added at concentrations of 0.2 M each, and the solution was stirred for 1 h to promote EDC/NHS coupling. Subsequently, CA was added at 0.16% (w/v) and

stirred for 10 min. The reacted BC pellicles were transferred to Petri dishes, frozen at −80 °C, and lyophilized for 48 h. The dried aerogels were heat-treated at 80 °C under humid conditions for 1 h to induce ester crosslinking between CA, BC, and CMC. The aerogels were then washed four times with cold water (15 min each) and freeze-dried again to obtain purified BC/CMC-NHS/CA aerogels.

For comparison, CMC-NHS/CA aerogels were prepared under the same conditions without BC, and BC aerogels were obtained by freeze-drying pristine BC pellicles without chemical treatment (−80 °C freezing, 48 h lyophilization).

To introduce the designed kirigami structures and fabricate various shapes of the adhesive, BC/CMC-NHS/CA aerogels (40 mm × 40 mm) were cut using a laser cutter (LaserPecker LP2, LaserPecker, USA).

4.4. Fluorescence-labeled polymer diffusion test

Fluorescein isothiocyanate (FITC)-labeled dextran with a molecular weight of 150 kDa was used as a model polymer to evaluate macromolecular diffusion into bacterial cellulose (BC). Cube-shaped BC samples (12 mm × 12 mm × 12 mm) were immersed in an aqueous FITC-dextran solution (0.005 mg mL^{-1}) and incubated for 24 h under gentle agitation at 100 rpm to allow diffusion of the polymer into the BC matrix. After diffusion, the BC cubes were sectioned through the center, and the resulting cross-sections were observed using a confocal laser scanning microscope (CLSM, K1-Fluo, Nanoscope Systems, Korea) at an excitation/emission wavelength of 488/525 nm. Fluorescence intensity distribution was quantitatively analyzed based on the acquired fluorescence images. Six lines were drawn across each cross-section at uniform intervals, and the fluorescence intensity along each line was measured using the plot profile function in ImageJ software (NIH, USA).

4.5. Fourier-transform infrared (FTIR) spectroscopy

FTIR analysis was performed using a spectrometer (Nicolet iS5, Thermo Fisher Scientific, USA) to confirm NHS ester formation and CA-induced ester crosslinking. The instrument was equipped with an attenuated total reflectance (ATR) module (ZnSe crystal plate, model 869-129000, Thermo Fisher Scientific, USA). Spectra were recorded in the range of 650–4000 cm^{-1} with a resolution of 4 cm^{-1}, averaging 32 scans per sample. Background spectra were collected using air as a reference.

4.6. Ferric-based colorimetric assay

To quantitatively evaluate the active NHS ester content, the color change induced by the complexation between hydrolyzed NHS ester and ferric ions was analyzed using a UV/vis spectrophotometer (Optizen, K Lab Co., Korea). The adhesive samples (10 mm × 10 mm) were weighed and then cut into four equal pieces. Each sample was placed in a 1.5 mL microcentrifuge tube containing 0.5 mL of distilled water and 0.05 mL of 2 N NaOH solution, followed by incubation at 60 °C for 10 min. After cooling on ice for 1 min, 0.75 mL of 0.85 N HCl solution was added and the mixture was centrifuged at 12 000 rpm for 15 min using a microcentrifuge (Micro 17TR,

Hanil Science Industrial Co., Korea) to precipitate the residual sheet pieces. Subsequently, 1 mL of the supernatant was reacted with 0.25 mL of 5 wt% FeCl$_3$ (ferric chloride anhydrous, ≥97%, Duksan, Korea) solution prepared in 0.1 N HCl, and the absorbance was measured at 500 nm. For all adhesive formulations listed in Table S1, the active NHS ester content (mmol g^{-1}) was determined based on a calibration curve constructed using NHS standard solutions with concentrations ranging from 0 to 0.25 mM.

4.7. Scanning electron microscopy (SEM)

The surface and cross-sectional morphologies of the aerogels, and the surface morphologies of the various tissues (porcine skin, heart, and lung) were examined using field-emission scanning electron microscopy (FE-SEM, SIGMA, Carl Zeiss, Germany). The samples were sputter-coated with platinum at 20 mA for 180 s prior to imaging, and observations were performed at an accelerating voltage of 15 kV.

4.8. Mechanical tests

To evaluate the mechanical properties under wet conditions, BC, CMC-NHS/CA, and BC/CMC-NHS/CA samples were cut into bar-shaped specimens (50 mm × 10 mm) and fully swollen in phosphate-buffered saline (PBS) solution for 6 h. Tensile tests were performed using a universal testing machine (UTM, GB/LRX Plus, Lloyd, UK) equipped with a 10 N load cell. The specimen thickness was measured prior to testing, and experiments were conducted with a gauge length of 30 mm, preload of 0.1 N, and crosshead speed of 2 mm min^{-1}. Cyclic tensile fatigue tests were conducted with a gauge length of 30 mm and a crosshead speed of 25 mm min^{-1}. All tensile measurements were performed on at least three replicate specimens ($n = 3$). The ultimate tensile strength (UTS) was determined as the maximum stress before fracture, and the elongation at break was obtained from the strain at failure.

Adhesion strength between the tissue adhesives and porcine tissues (skin, heart, and lung) was evaluated *via* lap-shear test using the same UTM. Prior to testing, tissues were rinsed with PBS and gently blotted to remove surface moisture. Square tissue adhesive samples (12 mm × 12 mm) were attached to the surface of porcine tissues (12 mm × 40 mm × 3 mm) and pressed for 10 s. Tests were conducted at a preload of 0.1 N and a crosshead speed of 25 mm min^{-1}. All adhesion tests were performed in triplicate ($n = 3$) for each condition. Shear strength (τ) was calculated by dividing the maximum load at failure (F_{max}) by the adhesion area (A):

$$\tau = \frac{F_{max}}{A}$$

where τ is the shear strength, F_{max} is the maximum load at failure, and A is the adhesion area.

To assess adhesion retention under simulated *in vivo* moist conditions, bonded specimens were sealed in plastic bags and stored for 1 h or 24 h before testing under the same conditions.

For cyclic loading tests, two pieces of porcine heart tissue (20 mm × 25 mm × 3 mm) were bonded using BC, CMC-NHS/CA,

or BC/CMC-NHS/CA aerogels (15 mm × 18 mm). The specimens were fixed in the UTM grips and subjected to repeated tensile loading at a crosshead speed of 100 mm min^{-1} and 20% strain (based on aerogel length).

To evaluate the high-deformation tolerance of the kirigami-designed adhesive, adhesive retention was examined on the lung tissue surface. BC/CMC-NHS/CA tissue adhesive with the kirigami structure (13 mm × 35.4 mm) were attached to porcine lung tissues (40 mm × 70 mm × 5 mm) and pressed for 10 s. The lung tissue was then elongated to 40% strain under a preload of 0.1 N and a crosshead speed of 25 mm min^{-1}. For comparison, the same test was conducted on aerogels of identical size without the kirigami design.

4.9. Quantification of polymer area fraction on the surface

The polymer area fraction on the aerogel surface was quantified using SEM images taken at identical magnifications. Images were analyzed using ImageJ. To distinguish polymer regions from pores, Phansalkar thresholding was applied to binarize the images, with polymer areas appearing white and pores black. The fraction of the white region within the total area was measured to calculate the polymer area fraction. Three different images per sample were analyzed.

4.10. *In vitro* cytocompatibility evaluation

NIH-3T3 fibroblasts were cultured in Dulbecco's Modified Eagle's Medium (DMEM, Gibco, USA) supplemented with 10% (v/v) fetal bovine serum (FBS, Gibco, USA) and 1% (v/v) Antibiotic–Antimycotic (Welgene, Korea) at 37 °C under a 5% CO_2 atmosphere. Circular BC and BC/CMC-NHS/CA aerogel discs (8 mm diameter) were sterilized by immersion in 70% (v/v) ethanol for 20 min, followed by UV irradiation for 3 h while air-drying in a clean bench. Cell suspensions (5×10^5 cells mL^{-1}) were seeded onto the aerogels (20 μL per sample) and allowed to attach for 10 min before adding 2 mL of medium. The culture medium was replaced daily.

Cell attachment and viability were evaluated using a live/dead assay. After 1 and 7 days of culture, samples were incubated with 500 μL of staining medium containing 6.7 μM Calcein AM (Max-view™, BIOMAX, Korea) and 15 μM propidium iodide (Max-view™, BIOMAX, Korea) for 20 min at 37 °C. The stained cells were observed using a confocal laser scanning microscope (CLSM, K1-Fluo, Nanoscope Systems, Korea) at excitation/emission wavelengths of 488/525 nm (live) and 561/593 nm (dead). Quantitative analysis was performed based on the acquired fluorescence images. Cells within a 1 mm × 1 mm region of interest at the center of each image were counted, and cell viability was calculated as the ratio of live cells to the total number of cells.

Cell metabolic activity was assessed using the Alamar Blue assay. After 1, 4, and 7 days, 500 μL of resazurin solution (alamarBlue™ Cell Viability Reagent, Invitrogen, USA) was added to each well and incubated for 2 h at 37 °C. Subsequently, 200 μL of the reaction solution was transferred to a 96-well plate, and fluorescence intensity was measured using a microplate reader (BioTek, USA) at Ex/Em = 540/590 nm.

4.11. Statistical analysis

All results were plotted using GraphPad Prism (version 8.0, GraphPad Software, USA). Statistical significance was analyzed using one-way ANOVA followed by Tukey's *post hoc* test, or a Student's *t*-test for two-group comparisons. Statistical significance was indicated as follows: $p < 0.05$ (*), $p < 0.01$ (**), $p < 0.001$ (***), and $p < 0.0001$ (****). No statistical significance was assumed for comparisons yielding $p \geq 0.05$ (n.s.). All data are presented as mean, with error bars representing the standard deviation (SD).

Author contributions

D. Hwang designed the experiments and revised the manuscript. K. Sung and D. Kang contributed to the characterization and discussion of data. S. Shin provided scientific guidance throughout, conceived the idea, designed the experiments, and wrote the manuscript. All authors made comments and approved the manuscript.

Conflicts of interest

There are no conflicts to declare.

Data availability

Further data are available from the corresponding author upon request.

The data supporting the findings of this study are available within the article and the supplementary information (SI). Supplementary information is available. See DOI: https://doi.org/10.1039/d5mh02244d.

Acknowledgements

Notes and references

1 T. B. Reece, T. S. Maxey and I. L. Kron, *Am. J. Surg.*, 2001, **182**, S40–S44.

2 S. Nam and D. Mooney, *Chem. Rev.*, 2021, **121**, 11336–11384.

3 Y. F. Ma, J. X. Yao, Q. Liu, T. Han, J. P. Zhao, X. H. Ma, Y. M. Tong, G. R. Jin, K. Qu, B. Q. Li and F. Xu, *Adv. Funct. Mater.*, 2020, **30**, 2001820.

4 Y. Li, G. H. Li, Y. Chen, X. T. Zhao, Y. T. Wang, J. Liu and Z. Li, *Adv. Funct. Mater.*, 2022, **32**, 2207306.

5 J. J. Wu, H. Yuk, T. L. Sarrafian, C. F. Guo, L. G. Griffiths, C. S. Nabzdyk and X. H. Zhao, *Sci. Transl. Med.*, 2022, **14**, eabh2857.

6 Z. W. Ma, G. Y. Bao and J. Y. Li, *Adv. Mater.*, 2021, **33**, 2007663.

7 S. N. Li, Y. Cong and J. Fu, *J. Mater. Chem. B*, 2021, **9**, 4423–4443.

8 V. Bhagat and M. L. Becker, *Biomacromolecules*, 2017, **18**, 3009–3039.

9 G. M. Taboada, K. S. Yang, M. J. N. Pereira, S. H. S. Liu, Y. S. Hu, J. M. Karp, N. Artzi and Y. H. Lee, *Nat. Rev. Mater.*, 2020, **5**, 310–329.

10 X. Y. Mao, H. Yuk and X. H. Zhao, *J. Mech. Phys. Solids*, 2020, **137**, 103863.

11 H. Yuk, C. E. Varela, C. S. Nabzdyk, X. Y. Mao, R. F. Padera, E. T. Roche and X. H. Zhao, *Nature*, 2019, **575**, 169–174.

12 J. Liu, S. T. Lin, X. Y. Liu, Z. Qin, Y. Y. Yang, J. F. Zang and X. H. Zhao, *Nat. Commun.*, 2020, **11**, 1071.

13 X. Ni, C. Chen and J. Y. Li, *Extreme Mech. Lett.*, 2020, **34**, 100601.

14 J. Sedó, J. Saiz-Poseu, F. Busqué and D. Ruiz-Molina, *Adv. Mater.*, 2013, **25**, 653–701.

15 A. H. Hofman, I. A. van Hees, J. Yang and M. Kamperman, *Adv. Mater.*, 2018, **30**, 1704640.

16 Y. H. Zhao, Y. Wu, L. Wang, M. M. Zhang, X. Chen, M. J. Liu, J. Fan, J. Q. Liu, F. Zhou and Z. K. Wang, *Nat. Commun.*, 2017, **8**, 2218.

17 H. A. Hegazy, H. H. Moon, D. H. Lee, S. H. Bhang, Y. C. Kim, C. S. Song and J. H. Kim, *Mater Adv*, 2023, **4**, 1989–1997.

18 S. P. Zustiak and J. B. Leach, *Biomacromolecules*, 2010, **11**, 1348–1357.

19 R. S. Labow, E. Meek and P. Santerre, *J. Biomater. Sci., Polym. Ed.*, 1999, **10**, 699–713.

20 P. A. Leggat, D. R. Smith and U. Kedjarune, *Anz J Surg*, 2007, **77**, 209–213.

21 P. Ferreira, J. F. J. Coelho and M. H. Gil, *Int. J. Pharmaceut.*, 2008, **352**, 172–181.

22 A. P. Duarte, J. F. Coelho, J. C. Bordado, M. T. Cidade and M. H. Gil, *Prog. Polym. Sci.*, 2012, **37**, 1031–1050.

23 M. Rahimnejad and W. Zhong, *RSC Adv.*, 2017, **7**, 47380–47396.

24 H. Lee, S. M. Dellatore, W. M. Miller and P. B. Messersmith, *Science*, 2007, **318**, 426–430.

25 J. Saiz-Poseu, J. Mancebo-Aracil, F. Nador, F. Busqué and D. Ruiz-Molina, *Angew. Chem., Int. Ed.*, 2019, **58**, 696–714.

26 V. Kanikireddy, K. Varaprasad, T. Jayaramudu, C. Karthikeyan and R. Sadiku, *Int. J. Biol. Macromol.*, 2020, **164**, 963–975.

27 S. W. Pan, Y. G. Li, X. R. Tong, L. Chen, L. Wang, T. Li and Q. Zhang, *Carbohyd. Polym.*, 2023, **301**, 120324.

28 J. Wang, J. Tavakoli and Y. H. Tang, *Carbohyd. Polym.*, 2019, **219**, 63–76.

29 K. M. Pasaribu, S. Ilyas, T. Tamrin, I. Radecka, S. Swingler, A. Gupta, A. G. Stamboulis and S. Gea, *Int. J. Biol. Macromol.*, 2023, **230**, 123118.

30 Y. Xue, Z. H. Mou and H. N. Xiao, *Nanoscale*, 2017, **9**, 14758–14781.

31 J. D. P. de Amorim, K. C. de Souza, C. R. Duarte, I. D. Duarte, F. D. S. Ribeiro, G. S. Silva, P. M. A. de Farias, A. Stingl, A. F. S. Costa, G. M. Vinhas and L. A. Sarubbo, *Environ. Chem. Lett.*, 2020, **18**, 851–869.

32 R. J. Hickey and A. E. Pelling, *Front. Bioeng. Biotech.*, 2019, **7**, 45.

33 J. C. Courtenay, M. A. Johns, F. Galembeck, C. Deneke, E. M. Lanzoni, C. A. Costa, J. L. Scott and R. I. Sharma, *Cellulose*, 2017, **24**, 253–267.

34 W. Liu, H. S. Du, M. M. Zhang, K. Liu, H. Y. Liu, H. X. Xie, X. Y. Zhang and C. L. Si, *ACS Sustainable Chem. Eng.*, 2020, **8**, 7536–7562.

35 T. Siripongpreda, B. Somchob, N. Rodthongkum and V. P. Hoven, *Carbohyd. Polym.*, 2021, **256**, 117506.

36 M. D. Fontes, A. B. Meneguin, A. Tercjak, J. Gutierrez, B. S. F. Cury, A. M. dos Santos, S. J. L. Ribeiro and H. S. Barud, *Carbohyd. Polym.*, 2018, **179**, 126–134.

37 C. H. Yang, C. A. Chen and C. F. Chen, *Sens. Actuators, B*, 2018, **265**, 506–513.

38 T. Nongnual, N. Butprom, S. Boonsang and S. Kaewpirom, *Int. J. Biol. Macromol.*, 2024, **267**, 131135.

39 W. J. Feng and Z. K. Wang, *Adv. Sci.*, 2023, **10**, 2303326.

40 M. A. P. Morais, M. Silva, M. Barros, P. Halley, Y. Almeida and G. Vinhas, *J. Appl. Polym. Sci.*, 2024, **141**, e56162.

41 R. L. Schnaar and Y. C. Lee, *Biochemistry*, 1975, **14**, 1535–1541.

42 C. Y. Chang, A. T. Chan, P. A. Armstrong, H. C. Luo, T. Higuchi, I. A. Strehin, S. Vakrou, X. P. Lin, S. N. Brown, B. O'Rourke, T. P. Abraham, R. L. Wahl, C. J. Steenbergen, J. H. Elisseeff and M. R. Abraham, *Biomaterials*, 2012, **33**, 8026–8033.

43 I. Strehin, Z. Nahas, K. Arora, T. Nguyen and J. Elisseeff, *Biomaterials*, 2010, **31**, 2788–2797.

44 X. Lin, Y. Liu, A. B. Bai, H. H. Cai, Y. J. Bai, W. Jiang, H. L. Yang, X. H. Wang, L. Yang, N. Sun and H. J. Gao, *Nat. Biomed. Eng.*, 2019, **3**, 632–643.

45 X. Y. Chen, H. Yuk, J. J. Wu, C. S. Nabzdyk and X. H. Zhao, *Proc. Natl. Acad. Sci. U. S. A.*, 2020, **117**, 15497–15503.

46 H. Yuk, J. J. Wu, T. L. Sarrafian, X. Y. Mao, C. E. Varela, E. T. Roche, L. G. Griffiths, C. S. Nabzdyk and X. H. Zhao, *Nat. Biomed. Eng.*, 2021, **5**, 1131–1142.

47 J. W. Yang, R. B. Bai, B. H. Chen and Z. G. Suo, *Adv. Funct. Mater.*, 2020, **30**, 1901693.

48 G. F. Picheth, C. L. Pirich, M. R. Sierakowski, M. A. Woehl, C. N. Sakakibara, C. F. de Souza, A. A. Martin, R. da Silva and R. A. de Freitas, *Int. J. Biol. Macromol.*, 2017, **104**, 97–106.

49 C. Li, Y. Qian, X. Zhang and R. Wang, *J. Mater. Chem. B*, 2025, **13**, 2469–2479.

50 D. Gan, Z. Huang, X. Wang, L. Jiang, C. Wang, M. Zhu, F. Ren, L. Fang, K. Wang and C. Xie, *Adv. Funct. Mater.*, 2020, **30**, 1907678.

51 M. P. Illa, C. S. Sharma and M. Khandelwal, *J. Mater. Sci.*, 2019, **54**, 12024–12035.

52 Y. P. Lu, X. Y. Xu and J. S. Li, *J. Mater. Chem. B*, 2023, **11**, 3338–3355.

53 P. Cruces, B. Erranz, F. Lillo, M. A. Sarabia-Vallejos, P. Iturrieta, F. Morales, K. Blaha, T. Medina, F. Diaz and D. E. Hurtado, *BMJ Open Respir. Res.*, 2019, **6**, 107.

54 J. D. Tang, J. Y. Li, J. J. Vlassak and Z. G. Suo, *Soft Matter*, 2016, **12**, 1093–1099.

55 R. K. Zhao, S. T. Lin, H. Yuk and X. H. Zhao, *Soft Matter*, 2018, **14**, 2515–2525.